Simulation of DC dual-laterolog measurements in complex formations: a Fourier series approach with non-orthogonal coordinates and self-adapting finite elements

Myung Jin Nam[1], David Pardo[2*], and Carlos Torres-Verdín[1]

[1] The University of Texas at Austin, USA

[2] Basque Center for Applied Mathematics (BCAM), Spain

*Formerly, at the University of Texas at Austin, USA

E-mail addresses: nmj1203@gmail.com, dzubiaur@gmail.com, and cverdin@uts.cc.utexas.edu

Running head: FEM simulation of 3D DLL measurements

ABSTRACT

Dual laterolog (DLL) makes use of a galvanic conduction principle to focus electrical currents into rock formations, thereby minimizing shoulder and borehole effects in the measurement of formation resistivity. The tool includes two separate focusing systems: deep-sensing (LLd) and shallow-sensing modes (LLs). Laterolog current-focusing systems were designed for operation primarily in vertical boreholes penetrating horizontal layers; only recently their design has been revised for operation in deviated wells in the presence of electrical anisotropy.

The objective of this paper is to simulate three-dimensional (3D) DLL measurements in dipping, invaded, and electrically anisotropic formations and to appraise the corresponding effects on apparent resistivity logs. Simulations are performed by combining the use of a Fourier series expansion in a non-orthogonal system of coordinates with an existing 2D goal-oriented higher-order self-adaptive *hp* finite-element method. This numerical algorithm yields accurate solutions in limited CPU time since only a few Fourier modes are needed to simulate practical applications. For the calculation of focused currents, we introduce an embedded post-processing method that incorporates a synthetic focusing principle to compute current intensities at each iterative step of optimal mesh refinements. Our numerical method accurately simulates 3D DLL measurements in rock formations that exhibit extreme contrasts of electrical resistivity.

Simulations indicate that LLs resistivity logs are more sensitive to both invaded and anisotropic layers than LLd resistivity logs. In deviated wells, shoulder-bed effects on apparent resistivity logs increase with an increase of dip angle, and are emphasized across thin conductive layers. Electrical anisotropy effects on apparent resistivity logs substantially increase with dip angle.

INTRODUCTION

The electrical resistivity of clay-free hydrocarbon-bearing rocks depends on pore volume, pore-volume connectivity, electrical resistivity of connate water, and interconnected pore volume occupied by connate water. That is why resistivity logs are widely used to calculate hydrocarbon saturation in combination with nuclear logs (Anderson, 2001). However, often resistivity logs fail to properly measure electrical resistivity because they are affected by invasion and shoulder-bed effects. It is therefore desirable to utilize a resistivity logging instrument with variable radial lengths of investigation while delivering measurements with high vertical resolution. Such is the purpose of Dual Laterolog (DLL) instruments, intended for operation in boreholes which are more electrically conductive than the surrounding rock formations.

Dual laterolog was developed based on early laterolog tools, the laterolog 3 (LL3) and the laterolog 7 (LL7), both of which were introduced by Doll (1951). It includes two separate focusing systems: deep-sensing (LLd) and shallow-sensing modes (LLs). For both systems, DLL comprises nine electrodes: one main and four outer bucking current electrodes and four monitoring (potential) electrodes. Intensities of bucking (or focusing) currents are automatically adjusted so that the current emitted by the main electrode flows preferentially in the horizontal direction toward the formation. This design condition allows the assessment of formation resistivity beyond invaded zones while minimizing shoulder and borehole effects. For the case of LLd, the main electrical current penetrates deeply into the formation whereas LLs is more sensitive to the near-borehole region. Although DLL operates usually at non-zero frequencies (from 10 Hz to 1000 Hz) in order to reduce contact-impedance electrical noise and interference from natural potentials, DLL is usually considered to be a DC measurement (Anderson, 2001).

A plethora of relevant work has been published on the numerical simulation of laterolog

measurements. Liu et al. (1999) evaluated invasion effects on DLL measurements for two-dimensional (2D) axisymmetric environments using a finite-element method (FEM), while Cozzolino et al. (2007) utilized a synthetic focusing method to determine the intensities of bucking currents in their 2D simulations. Lovell (1993) developed a simulation method based on the frequency-dependent partial differential equations of the current potential. Chen et al. (1998) applied the current potential concept to DC array-laterolog simulation. Yang et al. (2007) introduced a second-order FEM to improve the accuracy of simulated 2D frequency-dependent DLL measurements. In all of the aforementioned projects, DLL measurements were simulated for the specific case of vertical wells.

Deviated wells are nowadays widely used in hydrocarbon surveillance because they penetrate longer distances within hydrocarbon layers. Accurate evaluation of hydrocarbon-producing zones in deviated wells is a subject of increasing importance in formation evaluation. The only reliable way to quantify dip-angle effects on laterolog measurements is to utilize 3D software (e.g. Druskin et al., 1999; Newman and Alumbaugh, 2002; Davydycheva et al., 2003; Wang and Signorelli, 2004; Avdeev et al., 2002), since deviated wells involve 3D geometries. However, 3D simulation algorithms often fail to yield accurate solutions in a limited amount of CPU time because computational requirements increase dramatically as a result of the complexity of arbitrary 3D geometries.

The objective of this paper is twofold: (a) first, to introduce a new numerical algorithm to simulate DC laterolog measurements acquired in deviated wells that penetrate invaded and electrically anisotropic formations; (b) second, to appraise the relative influence of invasion, shoulder-bed, and electrically anisotropic effects on laterolog measurements acquired in deviated wells as a function of dip angle.

We simulate 3D DC-based DLL measurements with a method that combines the use of a

Fourier series expansion in a non-orthogonal system of coordinates with a 2D goal-oriented higher-order self-adaptive *hp* FEM (Pardo et al., 2006; *h* denotes the element size and *p* the polynomial order of approximation within each element). Our 3D numerical method yields accurate solutions in limited CPU times because only a few Fourier modes are needed (typically, below 10) to simulate DLL measurements in a non-orthogonal system of coordinates (Pardo et al., 2008). The simulation of DLL measurements is based on the specific commercial DLL tool configuration (Yang et al., 2007).

In the simulation of DLL measurements, intensities of bucking currents are determined based on the probed resistivity distribution so as to actively focus the main survey current into the formation, away from the borehole. To determine optimal intensities of bucking currents, it is customary to use a post-processing method (Cozzolino et al., 2007; Yang et al., 2007). In the *hp* grid refinement algorithm, intensities of bucking currents need to be updated within every step of optimal *hp* mesh refinements. To that end, we introduce an embedded post-processing method (EPPM) in which the *hp* algorithm guarantees optimal grids for the simulation of focused DLL measurements.

The remainder of this paper is organized as follows: we first describe the DLL under consideration. Subsequently, we provide technical details of our simulation method, specifically the Fourier FEM and EPPM. Next, numerical simulations of DLL measurements are described for synthetic formation models of variable complexity and penetrated by deviated wells. We conclude by summarizing the main technical observations stemming from the simulation work.

DUAL LATEROLOG (DLL)

The two focusing systems of DLL instruments provide different current paths (Fig. 1) and radial lengths of investigation. DLL incorporates nine electrodes, five current (A_0, A_1, A_1', A_2 and

$A_{2'}$) and four monitoring (potential) electrodes (M_1, M_2, $M_{1'}$ and $M_{2'}$) (Fig. 1). All electrodes are located symmetrically with respect to the main survey electrode A_0 that emits a current of intensity equal to I_0. In LLd, the five current electrodes emit current with the same polarity but different intensities to focus the main survey current. By contrast, only three electrodes (namely, A_0, A_1 and $A_{1'}$) emit currents in LLs and the emitted currents return to the remaining, reversely polarized electrodes A_2 and $A_{2'}$.

Together with the two focusing systems, DLL incorporates a micro-spherically focused device (MicroSFL) used to measure the resistivity of the invaded zone and to detect bed boundaries. DLL tools are designed mainly with three objectives: small borehole effect, high vertical resolution, and three well-distributed radial lengths of investigation corresponding to LLd, LLs and MicroSFL, respectively (Anderson 2001). DLL tools manufactured by different service companies work in slightly different ways, possibly due to different monitoring conditions and different dimensions (e.g. Anderson, 2001; Cozzolino et al., 2007; Yang et al., 2007). With the specific tool configuration of a commercial DLL tool (Fig. 1), we simulate the two focusing systems of DLL invoking the monitoring conditions described by Cozzolino et al (2007).

Monitoring conditions

For the simulation of DLL measurements, we compute the intensities of currents emitted by the four bucking electrodes, A_1, $A_{1'}$, A_2 and $A_{2'}$ (I_1, $I_{1'}$, I_2 and $I_{2'}$, respectively). Subsequently, the intensity of current emitted by the main electrode, A_0, is set to I_0 = 1A. The four unknowns, I_1, $I_{1'}$, I_2 and $I_{2'}$ are determined in such a way that potential gradients between two pairs of monitoring electrodes are null for both LLd and LLs operating modes, i.e.

$$V(M_1) = V(M_2) \text{ and } V(M_{1'}) = V(M_{2'}). \quad (1)$$

In the vicinity of monitoring electrodes, the above conditions impose no current flow in the vertical direction thereby causing the main survey current to enter the formation in the horizontal direction. There are two additional relationships between I_1 and I_2 , and $I_{1'}$ and $I_{2'}$, which can be expressed for LLd and LLs operating modes, respectively, as

$$I_2 = (I_1 + c) \text{ and } I_{2'} = (I_{1'} + c), \text{ and} \quad \text{(for LLd)} \quad (2)$$

$$I_2 = -(I_1 + c) \text{ and } I_{2'} = -(I_{1'} + c), \quad \text{(for LLs)} \quad (3)$$

where c is a parameter representing either: (a) an additional amount of current emitted by the outer guard electrodes A_2 and $A_{2'}$ with respect to the adjacent guard electrodes A_1 and $A_{1'}$, respectively (LLd), or (b) additional return of currents for both A_2 and $A_{2'}$ (LLs). The parameter c is set to 0.5 for the LLs operating mode, since all emitted currents should return to the current return electrodes (A_2 and $A_{2'}$). For the LLd operating mode, the survey current could be over-focused or under-focused depending on the value of c, since c is the additional amount of current emitted by the outer guard electrodes. Following Cozzolino et al. (2007), we select c = 0.5 for the LLd operating mode.

Description of the DLL tool

In computer-aided simulation of DLL measurements, Dirac delta functions are commonly used to represent source electrodes (Cozzolino et al., 2007) even though actual electrodes are finite in size. To simulate DLL measurements, we use realistic finite-size electrodes with practical values of electrode dimensions and resistivities. Moreover, employing finite-source

electrodes is consistent with using a self-adaptive algorithm: a load similar to a Dirac delta function should not be used in combination with any self-adaptive algorithm since the corresponding exact solution possesses infinite energy.

For the simulation of DLL measurements, we implement a specific commercial DLL tool configuration (Fig. 1). Each simulated electrode is positioned at the same location with the same vertical dimension as that of the commercial DLL tool. When simulating LLd measurements, we assume a current return electrode located at infinity and hence do not include its physical dimensions in the simulation. We assume that the resistivity of all the electrodes is 10^{-5} ohm-m, while the resistivity of the insulator (the rest of the DLL tool except for the nine electrodes) is 10^{5} ohm-m. Thus, the resistivity contrast at the interfaces between electrodes and insulator is 10^{10}.

SIMULATION METHOD

Fourier series expansion in a non-orthogonal system of coordinates

The electrostatic equation in a spatial domain Ω, which governs DC resistivity logging applications is given by

$$\nabla \cdot \left(\bar{\bar{\boldsymbol{\sigma}}} \nabla u \right) = \nabla \cdot \mathbf{J}^{imp}, \tag{4}$$

where $\bar{\bar{\boldsymbol{\sigma}}}$ is the conductivity tensor, $\mathbf{J}^{imp}$ is the impressed electric current density measured in A/m^2 and u is the electrostatic potential measured in volts. On the domain boundary far from the electrode, denoted by Γ_D, where the electric potential is approximately zero, we assign a homogeneous Dirichlet boundary condition (BC), $u\big|_{\Gamma_D} = 0$.

Multiplication of the electrostatic equation 4 with a test function $v \in H^1_D(\Omega) = \{u \in L^2(\Omega)$:

$u|_{\Gamma_D} = 0$, $\nabla u \in \boldsymbol{L}^2(\Omega)\}$, which is the space of admissible solutions, and integrating by parts over the computational domain Ω, gives rise to the resulting variational formulation:

$$\begin{cases} \text{Find } u \in u_D + H_D^1(\Omega) \text{ such that:} \\ \int_\Omega \bar{\bar{\sigma}} \nabla u \nabla v dV = \int_\Omega \nabla \cdot \mathbf{J}^{imp} v dV + \int_{\Gamma_N} g v dS, \quad \forall v \in H_D^1(\Omega), \end{cases} \tag{5}$$

where u_D is a lift (typically $u_D = 0$), $g = (\bar{\bar{\sigma}} \nabla u) \cdot \mathbf{n}$ is a prescribed flux defined on Γ_N, $\mathbf{n}$ is the unit normal outward (with respect to Ω) vector.

For a deviated well, Pardo et al. (2008) suggested the following non-orthogonal coordinate system $\boldsymbol{\zeta} = (\zeta_1, \zeta_2, \zeta_3)$ in terms of the Cartesian coordinate system $\mathbf{x} = (x_1, x_2, x_3)$ (Fig. 2):

$$\begin{cases} x_1 = \zeta_1 \cos \zeta_2 \\ x_2 = \zeta_1 \sin \zeta_2 \\ x_3 = \zeta_3 + \theta_0 f_1(\zeta_1) \cos \zeta_2 \end{cases}, \tag{6}$$

where $\theta_0 = \tan\theta$, θ is the dip angle, and f_1 is defined for ρ_1 and ρ_2 as

$$f_1(\zeta_1) = \begin{cases} 0 & \zeta_1 < \rho_1 \\ \dfrac{\zeta_1 - \rho_1}{\rho_2 - \rho_1} \rho_2 & \rho_1 \le \zeta_1 \le \rho_2 \\ \zeta_1 & \zeta_1 > \rho_2 \end{cases}, \tag{7}$$

where ρ_1 is the interface between subdomains I and II, and ρ_2 is the interface between subdomains II and III shown in Fig. 2b (note that the change of coordinates degenerates for a horizontal well, i.e., $\theta_0 \rightarrow \infty$ as $\theta \rightarrow 90°$). Subdomain I, being part of the borehole, includes the

DLL logging instrument while subdomain III corresponds to the formation. Subdomain II, the remainder part of the borehole except for subdomain I, "glues" subdomain I with subdomain III in a linear way as indicated by equations 6 and 7, such that the resulting system of coordinates is globally continuous, bijective, and with a positive Jacobian.

In this non-orthogonal system of coordinates, a deviated well with a dip angle equal to θ (Fig. 2a) has material properties that are invariant with respect to the quasi-azimuthal direction ζ_2. We can efficiently simulate DLL measurements in a deviated well with a Fourier series expansion (Appendix A) because the metric (Aris, 1962) associated with the change of coordinates from a reference grid to the physical 3D geometry is decomposed in terms of only five Fourier modes in subdomain II in the quasi-azimuthal direction ζ_2, while in terms of only one and three Fourier modes in subdomains I and III, respectively, (Pardo et al., 2008). In other words, the resulting formulation in deviated wells consists of a sequence of coupled problems (constituting the corresponding 3D problem), which has a very special interaction among the various 2D problems. Specifically, each 2D problem only interacts (couples) with a maximum of five 2D problems, which results in a penta-diagonal structure for the associated stiffness matrix (Appendix A, i.e., equation A-11). Furthermore, the maximum interaction that occurs among five different 2D problems takes place only in subdomain II. In subdomain III, an interaction occurs only among three 2D problems, while in subdomain I no interaction occurs (Appendix A). This sparsity of the resulting stiffness matrix is the major advantage of the formulation developed in this paper over more traditional 3D formulations.

Embedded post-processing method (EPPM)

When simulating DLL measurements, the main obstacle is the determination of the intensities of bucking currents needed to impose active focusing conditions (equations 1 through 3). It is

common practice to use a post-processing method that computes the intensities of bucking currents based on the superposition principle, and to impose the focusing conditions after computing the responses of each different source electrode (Cozzolino et al., 2007, Yang et al., 2007).

If the post-processing technique is applied directly to the individual solutions derived from adaptive methods, the post processing method will fail because optimal grids constructed dynamically with adaptive methods for individual sources are not optimal for DLL measurements; they are only optimal for each individual source. As a remedy to this problem, we use EPPM, in which a post-processing algorithm based on a synthetic focusing method (Cozzolino et al., 2007) is applied at every step of mesh refinements and thus, is embedded in the *hp* adaptive algorithm.

EPPM solves one problem with five right-hand sides (RHSs, corresponding to individual electrodes activated while the remaining four are disabled) on each grid in order to compute the intensities of current electrodes using the synthetic focusing method. Using the main current together with four bucking currents for the calculated intensities as DLL source, the *hp* algorithm performs optimal mesh refinements for DLL measurements. In this manner, the *hp* algorithm with EPPM generates a sequence of optimal grids that converge exponentially and that ultimately provide a small error (below 1% in this study) in the quantity of interest (apparent resistivity in this study).

Synthetic focusing

Using the superposition principle, total potentials ($V(M_i)$) at each monitoring electrode (M_i) can be expressed as:

$$
\begin{aligned}
V(M_2) &= I_2V_{2,2} + I_1V_{2,1} + V_{2,0} + I_{1'}V_{2,1'} + I_{2'}V_{2,2'},\\
V(M_1) &= I_2V_{1,2} + I_1V_{1,1} + V_{1,0} + I_{1'}V_{1,1'} + I_{2'}V_{1,2'},\\
V(M_{1'}) &= I_2V_{1',2} + I_1V_{1',1} + V_{1',0} + I_{1'}V_{1',1'} + I_{2'}V_{1',2'}, \text{ and}\\
V(M_{2'}) &= I_2V_{2',2} + I_1V_{2',1} + V_{2',0} + I_{1'}V_{2',1'} + I_{2'}V_{2',2'},
\end{aligned} \tag{8}
$$

where $V_{i,j}$ is potential on M_i due to only the current with unit intensity acting on a current electrode A_j while the remaining current electrodes are disabled. Thus, equation 1 becomes

$$
\begin{aligned}
&I_2V_{1,2} + I_1V_{1,1} + V_{1,0} + I_{1'}V_{1,1'} + I_{2'}V_{1,2'} = I_2V_{2,2} + I_1V_{2,1} + V_{2,0} + I_{1'}V_{2,1'} + I_{2'}V_{2,2'}, \text{ and}\\
&I_2V_{1',2} + I_1V_{1',1} + V_{1',0} + I_{1'}V_{1',1'} + I_{2'}V_{1',2'} = I_2V_{2',2} + I_1V_{2',1} + V_{2',0} + I_{1'}V_{2',1'} + I_{2'}V_{2',2'}.
\end{aligned} \tag{9}
$$

From equation 9 together with equation 2 for LLd or equation 3 for LLs, we obtain a linear system of four equations with four unknowns. The solution of the two linear systems yields the intensities of bucking currents, I_1, $I_{1'}$, I_2 and $I_{2'}$ for LLd and LLs, respectively. Subsequently, apparent resistivities (ρ_a) are calculated from the ohmic drop of the current I_0 = 1A between a monitoring electrode and the reference potential electrode N, i.e.

$$
\rho_a = K\frac{V - V_N}{I_0} \approx KV_{avr}, \tag{10}
$$

where K is the tool constant (K_{LLd} for LLd and K_{LLs} for LLs), V_N is usually assumed to be negligible since N is often located relatively far away from A_0, and V can be considered as the average of the potentials (V_{avr}) measured at the four monitoring electrodes. The tool constraint K can be determined in a homogeneous medium where the measured apparent resistivity should be

equal to the medium resistivity (Chen et al., 1998).

We choose apparent resistivity as the quantity of interest (L), for which the *hp* algorithm generates optimal grids, that is:

$$L(u) = \rho_a = \frac{K}{4}\left(\frac{1}{|\Omega_{M_1}|}\int_{\Omega_{M_1}} u(x)dx + \frac{1}{|\Omega_{M_{1'}}|}\int_{\Omega_{M_{1'}}} u(x)dx + \frac{1}{|\Omega_{M_2}|}\int_{\Omega_{M_2}} u(x)dx + \frac{1}{|\Omega_{M_{2'}}|}\int_{\Omega_{M_{2'}}} u(x)dx \right), \quad (11)$$

where $|\Omega_{M_i}| = \int_{\Omega_{M_i}} 1dx$ and we have considered the relationship in equation 10.

NUMERICAL RESULTS

Verification of the 2D *hp* algorithm

In order to verify the EPPM, we consider a 2D model for which the corresponding DLL apparent resistivity logs are described in Cozzolino et al. (2007). The model consists of three horizontal layers with resistivities equal to 1, 0.1 and 10 ohm-m from top to bottom. Resistivity and radius of the borehole are 5 ohm-m and 0.1 m, respectively. To simulate DLL measurements for the 2D model, EPPM is applied to a 2D self-adaptive goal-oriented *hp*-FEM algorithm (Pardo et al., 2006), which has already been validated against existing analytical solutions (Paszynski et al., 2005). Cozzolino et al. (2007) employed Dirac delta functions to model sources. Since Dirac delta sources produce solutions with infinite energy that cannot be employed in combination with self-adaptive gridding algorithms, in this paper we consider electrodes with size equal to 0.01 m × 0.01 m at 0.01 m in the radial direction with the same resistivity as that of the borehole mud. In addition, we assume the same spacing between the centers of electrodes described by Cozzolino et al. (2007).

Figure 3 compares the results obtained by Cozzolino et al. (2007) to those obtained with the

2D hp algorithm for the 2D model described above. The agreement is very good showing only negligible differences, which can be explained either by the different way of modeling sources or by the fact that the solutions have been simulated on different grids; our solutions are simulated on optimal grids generated by the 2D self-adaptive goal oriented *hp*-FEM algorithm.

Model formation

Figure 4 shows a five-layer formation model penetrated by a deviated well, which is used for the remaining numerical simulations considered in this paper. The model includes five horizontal layers with resistivities equal to 100, 5, 1000, 0.5, and 100 ohm-m from top to bottom, respectively. Thicknesses of the second, third and fourth layers are 2, 4 and 3 m, respectively. Borehole radius and resistivity are equal to of 0.1 m and 0.1 ohm-m, respectively To display numerical results, we use the center point of the DLL tool to reference the relative depth of DLL measurements with respect to the probed formation; the relative depth is equal to 0 at the interface between the second and third layers.

Vertical well

We first test our 3D simulation algorithm on a 0° deviated (vertical) well penetrating the five-layer formation model (Fig. 4). The non-orthogonal system of coordinates in equation 6 for a vertical well is identical to a system of cylindrical coordinates because the dip angle of a vertical well, θ, is 0°. Therefore, the 3D formulation for a 0° deviated well can be reduced to a 2D formulation in the system of cylindrical coordinates. To verify this, we simulate DLL measurements employing both the 3D algorithm with one Fourier mode and the 2D algorithm verified in the previous section. Both algorithms give the same results (see Fig. 5) up to more than 8 digits of accuracy for LLd (black) and LLs (light gray) apparent resistivity logs in the

vertical well without presence of invasion (dashed line) (the comparison between them is not shown here).

In Fig. 5, both LLd and LLs resistivity logs for a formation without invasion show significantly good vertical resolution, since they are both close to the actual resistivities of the formation even though the largest resistivity contrast of the formation is more than 10^3. Across the conductive second and fourth layers, LLd apparent resistivities depart from actual formation resistivities. This behavior is attributed to shoulder-bed effects in conductive layers for galvanic tools, which can be viewed as the opposite of shoulder-bed effect in resistive layers for the case of induction tools.

In order to validate the performance of the hp-algorithm, in Fig. 6 we display amplifications of the corresponding optimal grid for LLd measurements at a depth of 4 m in the formation without presence of invasion. The amplifications are made toward a singular point $(\rho, z) = (-1$ m, 4 m), where three materials (namely, the borehole, the third and forth layers) with highly varying resistivities (0.1, 1000, 0.5 ohm-m, respectively) meet. For further performance on the *hp* algorithm, interested readers are referred to Pardo et al. (2006), Demkowicz (2007) and Demkowicz et al. (2008).

Invasion

We consider invaded zones with resistivities equal to 50 and 5 ohm-m in the third and fourth layers, respectively. The invaded zone in the third layer is more conductive than its virgin formation while that in the fourth layer is more resistive. When the radial length of invasion is 0.1 m (♦; Fig. 5), LLs logs are more influenced by invasion than LLd logs (the corresponding effect on apparent resistivity is almost twice as large) in the fourth conductive layer, while no significant difference is observed between effects of invasion on LLs and LLd apparent

resistivities across the third resistive layer. If the radial length of invasion increases to 0.8 m (▲), both LLd and LLs apparent resistivities are much closer to the resistivities of the invasion zones in both layers; LLs apparent resistivities are slightly closer to the resistivities of the invasion zones than LLd apparent resistivities since LLd was designed to investigate deeper than LLs.

Anisotropy

Electrical anisotropy is usually observed in sedimentary layers whose conforming grains have elongated shapes in the parallel direction to the plane of deposition, and therefore whose pore structure makes electric current flow more efficient in the parallel than in the vertical direction to the bedding plane. This type of electrical anisotropy is referred to as transversely isotropic (TI) in which the horizontal resistivity (resistivity in the parallel direction) is different from the vertical resistivity (resistivity in the vertical direction). DLL measurements are affected by TI electrical anisotropy, even though the first DLL tools were assumed to be almost insensitive to vertical resistivity, and therefore used to measure the horizontal resistivity because emitted currents are focused by bucking currents to flow laterally deep into the probed formation (Anderson, 2001).

Electrical anisotropy, that is TI, is included in the third and fourth layers. Vertical resistivities in those layers are set to 10000 and 5 ohm-m, respectively, which are ten times larger than the corresponding horizontal resistivities (1000 and 0.5 ohm-m in the third and fourth layers, respectively). Across the center of the fourth anisotropic, conductive layer, we observe that LLs apparent resistivities are affected by anisotropy (increased by 30.5%; Fig. 7), while the effects of anisotropy on LLd apparent resistivity logs are negligible (decreased by 7.9% rather than increased). On the other hand, both LLd and LLs apparent resistivities in the third (resistive) layer are increased by up to 29.8% and 39.6%, respectively, because of TI anisotropy.

Verification of the 3D *hp* algorithm

In order to verify the accuracy and reliability of the 3D *hp* algorithm, in addition to the above comparison between results for the vertical well derived from 2D and 3D algorithms, respectively, we simulate DLL measurements acquired in a deviated well that penetrates a homogeneous formation with resistivity equal to 1 or 1000 ohm-m (Fig. 8). Note that, even though the two models comprise a homogeneous formation, we model them as full 3D problems, since we situated the DLL tool (with realistic material properties and dimensions) in a deviated borehole penetrating the formation. In particular, solutions for the 3D problem should coincide with the corresponding axial-symmetric solution for a vertical well because the resistivity of the formation is homogeneous. We compute DLL apparent resistivities for each formation (having a resistivity equal to 1 or 1000 ohm-m) with dip angles of 30° and 60°, respectively, and compare them to the reference 2D solutions for the axial-symmetric case of a vertical (0° deviated) well.

Figure 9 shows the convergence history for LLd (in black) and LLs (in light gray) apparent-resistivity logs for the two problems in log-log scale. For the 60° deviated well (dashed line with ▲) in both formations, we obtain solutions with a relative error below 1% with respect to the exact (2D) solution when using 7 Fourier modes or less for both LLs and LLd modes, while for the 30° deviated well (solid line with ♦) the number of Fourier modes needed for convergence is reduced to only three.

To further verify the 3D algorithm, in Fig. 10 we show the convergence history of LLd apparent-resistivity readings for a 45° deviated well penetrating the five-layer formation after computing the apparent resistivities with various numbers of Fourier modes for the solution. Assuming that LLd resistivities computed with nine Fourier modes are a fully converged solution, we compare LLd resistivities computed with one, three, five and seven Fourier modes, respectively (Figs. 10a, b, c and d), against the solution with nine Fourier modes. When using

one Fourier modal coefficient (Fig. 10a), LLd resistivity logs exhibit noticeable discrepancies from the reference solution, especially across conductive layers. LLd resistivity logs calculated with three Fourier modes (Fig. 10b) show relatively small discrepancies except near the boundaries of both the third and fifth layer. When five Fourier modes are used (Fig. 10c) to perform the simulation, we obtain improved LLd apparent-resistivity readings in the vicinity of layer boundaries. Using seven Fourier modes (Fig. 10d) yields the same result as that of the exact (reference) solution.

Deviated well

Figure 11 shows simulation results for 60° (►), 45° (▲) and 10° (♦) deviated wells together with a 0° deviated (vertical) well. Simulated apparent resistivities for the 10° deviated well are similar to those for the vertical well since the dip angle is small. When the dip angle increases to 45°, LLd apparent resistivities across the resistive third layer slightly decrease near bed boundaries. Close to the center of the layer, the difference between apparent resistivities for the vertical and 45° deviated wells becomes even smaller. On the other hand, LLd apparent resistivities across the conductive second and fourth layers increase; the differences are larger in the thinner second layer than in the fourth layer. This behavior is attributed to increased shoulder-bed effects. In deviated wells, more current flows into shoulder beds than in vertical wells because the main survey current in LLd is focused to flow deep into the formation in the plane perpendicular to the DLL tool. More current will flow into the adjacent layers than for the case of a vertical well when the tool is situated in a more deviated well or in a thinner layer; the more the survey current flows into the adjacent layers the larger the corresponding effect on DLL apparent resistivities.

LLs apparent resistivities for the 45° deviated well show almost the same resistivities as those

for the vertical wells at the center of the fourth conductive layer even though LLd resistivities exhibit increased values because the radial length of investigation is shorter in LLs than in LLd. In both LLd and LLs apparent resistivity logs, the effects of dip angle are more emphasized in the 60° deviated well than in the 45° deviated well.

Invasion

For both 45° and 60° deviated wells, we consider invasion with a radial length of 0.1 m in the third and fourth layers with resistivities of 50 and 5 ohm-m, respectively, as in the case of the vertical well. For both 45° (black) and 60° (light gray) deviated wells (Fig. 12), the overall characteristic of invasion effects on DLL apparent resistivity logs simulated in deviated wells are similar to those of the vertical well (Fig. 5); LLs apparent resistivity logs (Figs. 12b and 12d) are distorted by presence of invasion more than LLd apparent resistivity logs (Figs. 12a and 12c) across the conductive layer.

Anisotropy

To investigate effects of dip angle across electrically anisotropic layers, we simulate DLL apparent resistivities for 60° and 45° deviated wells in an electrically TI anisotropic formation, and compare them in Fig. 13 to those simulated across the isotropic formation. The third and fourth layers have vertical resistivities of 10000 and 5 ohm-m, respectively, as discussed previously. Both LLs (black) and LLd simulated apparent resistivities (light gray) across the resistive third layer are closer to the vertical resistivities in the deviated wells (Fig. 13) than in the vertical well (Fig. 7). Even though effects of electrical anisotropy on LLd readings in the vertical well are negligible in the fourth conductive layer, we observe effects of anisotropy on LLd apparent resistivity logs in a 60° deviated well (Table 1). Apparent resistivities across the

third and fourth layers for the 60° deviated well (Fig. 13b) are closer to the corresponding vertical resistivities than those for the 45° deviated well (Fig. 13a), indicating larger effects due to anisotropy on DLL measurements (Table 1). We conclude that the effect of anisotropy on apparent-resistivity logs increases with dip angle. This behavior is attributed to the fact that relatively more current flows in the vertical direction and that the latter is more affected by the vertical resistivities with increasing dip angle.

CONCLUSIONS

We have successfully simulated 3D DLL measurements in dipping, invaded, and anisotropic formations by combining the use of a Fourier series expansion in a non-orthogonal system of coordinates with a 2D goal-oriented higher-order self-adaptive *hp* finite-element method. Moreover, an embedded post-processing technique was introduced to compute the intensities of focused currents in combination with optimal grid refinements conducted by the *hp* FEM algorithm. Numerical results confirm that our method accurately simulates 3D DLL measurements in formations exhibiting extreme contrasts of electrical resistivity. It was found that LLs apparent resistivities are more sensitive to both invaded and anisotropic layers than LLd apparent resistivities. In deviated wells, shoulder-bed effects are more significant than in vertical wells because focused laterolog currents partially flow into shoulder beds. The increase of shoulder-bed effects is more clearly appreciated across thin layers and/or in highly deviated wells. Furthermore, electrical anisotropy effects increase with dip angle due to increased current flow in the vertical direction. Numerical simulation of laterolog measurements is necessary to reliably diagnose and quantify the effect of well deviation angle on the interpretation of formation resistivity.

ACKNOWLEDGEMENTS

The work reported in this paper was funded by the University of Texas at Austin's Research Consortium on Formation Evaluation, jointly sponsored by Anadarko, Aramco, Baker Atlas, BHP-Billiton, BP, British Gas, Chevron, ConocoPhilips, ENI E&P, ExxonMobil, Halliburton, Hydro, Marathon, Mexican Institute for Petroleum, Occidental Petroleum, Petrobras, Schlumberger, Shell E&P, Statoil, TOTAL, and Weatherford International Ltd.

APPENDIX A

Fourier series expansion in a non-orthogonal system of coordinates for deviated wells

The change of coordinates in equation 6 can be described by the mapping $\mathbf{x} = \psi(\boldsymbol{\zeta})$, which is bijective, with positive Jacobian determinant, and globally continuous (Pardo et al., 2008). Given an arbitrary scalar-valued function h, we denote $\tilde{h} := h \circ \psi$ and thus, using the chain rule, we obtain

$$\nabla u = \sum_{i,n=1}^{3} \frac{\partial \tilde{u}}{\partial \zeta_n} \frac{\partial \zeta_n}{\partial x_i} \mathbf{e}_{x_i} = \mathbf{J}^{-1T} \frac{\partial \tilde{u}}{\partial \boldsymbol{\zeta}}, \tag{A-1}$$

where $\mathbf{e}_{x_i}$ is the unit vector in the x_i-direction, $\frac{\partial \tilde{u}}{\partial \boldsymbol{\zeta}}$ is the vector with the n-th component being $\frac{\partial \tilde{u}}{\partial \zeta_n}$, and the Jacobian matrix given by

$$\mathbf{J} = \left\{ \frac{\partial x_i}{\partial \zeta_j} \right\}_{i,j=1,2,3} = \begin{pmatrix} \cos\zeta_2 & -\zeta_1 \cos\zeta_2 & 0 \\ \sin\zeta_2 & \zeta_1 \cos\zeta_2 & 0 \\ \theta_0 f_1' \cos\zeta_2 & -\theta_0 f_1 \sin\zeta_2 & 1 \end{pmatrix}, \tag{A-2}$$

where ζ_1, ζ_2, ζ_3 and θ_0 are the same as those used in equation 6, and f_1 is defined in equation 7. Equation 5 can be transformed into the non-orthogonal coordinate system of $\boldsymbol{\zeta}$, and expressed as

$$\begin{cases} \text{Find } \tilde{u} \in \tilde{u}_D + \tilde{H}_D^1(\widetilde{\Omega}) \text{ such that:} \\ < \dfrac{\partial \tilde{v}}{\partial \boldsymbol{\zeta}}, \tilde{\tilde{\boldsymbol{\sigma}}}_{NEW} \dfrac{\partial \tilde{u}}{\partial \boldsymbol{\zeta}} >_{L^2(\widetilde{\Omega})} = < \tilde{v}, \tilde{f}_{NEW} >_{L^2(\widetilde{\Omega})} + < \tilde{v}, \tilde{g}_{NEW} >_{L^2(\widetilde{\Gamma}_N)} \quad \forall \tilde{v} \in \tilde{H}_D^1(\widetilde{\Omega}), \end{cases} \tag{A-3}$$

where $\widetilde{\Omega} = \Omega \circ \psi$, and $< , >_{L^2(\widetilde{\Omega})}$ is the L^2-inner product of two arbitrary (possibly complex- and vector-valued) functions h_1 and h_2 such that

$$< h_1, h_2 >_{L^2(\widetilde{\Omega})} = \int_{\Omega} h_1^* h_2 d\zeta_1 d\zeta_2 d\zeta_3 , \tag{A-4}$$

and $\tilde{H}^1_D(\tilde{\Omega}) = \{\tilde{u} \in L^2(\widetilde{\Omega}) : \tilde{u}|_{\tilde{\Gamma}_D} = 0, \mathbf{J}^{-1T} \frac{\partial \tilde{u}}{\partial \zeta} \in \boldsymbol{L}^2(\widetilde{\Omega})\}$, $\tilde{\bar{\bar{\sigma}}}_{NEW} := \mathbf{J}^{-1} \tilde{\bar{\bar{\sigma}}} \mathbf{J}^{-1T} |\mathbf{J}|$, $\tilde{f}_{NEW} := \tilde{f} |\mathbf{J}|$ (f = $\nabla \cdot \mathbf{J}^{imp}$) and $\tilde{g}_{NEW} := \tilde{g} |\mathbf{J}_S|$, where $|\mathbf{J}|$ is the determinant of the Jacobian associated with the change of variables, and $|\mathbf{J}_S|$ is $|\mathbf{J}|$ restricted to $\widetilde{\Gamma}_N$ (Pardo et al., 2008).

In the new non-orthogonal system of coordinates described above, any function ω is periodic (with period 2π) with respect to ζ_2 (Pardo et al., 2008), and can be expressed in terms of its Fourier series expansion as

$$\omega = \sum_{l=-\infty}^{l=\infty} \omega_l e^{jl\zeta_2} = \sum_{l=-\infty}^{l=\infty} F_l(\omega) e^{jl\zeta_2} , \tag{A-5}$$

where $e^{jl\zeta 2}$ are the modes, $\omega_l = F_l(\omega) = \frac{1}{2\pi} \int_0^{2\pi} \omega e^{-jl\zeta_2} d\zeta_2$ are the modal coefficients that are independent of ζ_2, and $F_l(\omega)$ is the l-th Fourier modal coefficient, ω_l.

Using the Fourier series expansion representation for u, $\bar{\bar{\sigma}}_{NEW}$ and f_{NEW} (in the remainder of the paper, the symbol '~' is omitted for convenience) and selecting a mono-modal test function $v = v_k e^{jk\zeta_2}$, the variational problem A-3 can be reduced by orthogonality of the Fourier modes in L^2 to

$$\begin{cases} \text{Find } u = \sum_l F_l(u) e^{jl\zeta_2} \in \sum_l F_l(u_D) e^{jl\zeta_2} + H_D^1(\Omega) \text{ such that:} \\ \sum_{l=k-2}^{l=k+2} < F_k\left(\dfrac{\partial v}{\partial \boldsymbol{\zeta}}\right), F_{k-l}\left(\bar{\bar{\boldsymbol{\sigma}}}_{NEW}\right) F_l\left(\dfrac{\partial u}{\partial \boldsymbol{\zeta}}\right) >_{L^2(\Omega_{2D})} \\ \qquad = \left\langle F_k(v), F_k(f_{NEW}) \right\rangle_{L^2(\Omega_{2D})} + \left\langle F_k(v), F_k(g_{NEW}) \right\rangle_{L^2(\Gamma_N(\Omega_{2D}))} \quad \forall F_k(v) e^{jk\zeta_2} \in H_D^1(\Omega), \end{cases}$$

(A-6)

where $\Omega_{2D} = \{(\zeta_1, \zeta_2, \zeta_3) \in \Omega : \zeta_2 = 0\}$, the infinite series in terms of l has been reduced for each k to a finite sum with at most five terms, namely $l = k - 2, \ldots, k + 2$ because $F_{k-l}(\bar{\bar{\boldsymbol{\sigma}}}_{NEW}) = 0$ if $| k - l | > 2$ (Pardo et al., 2008), and

$$F_k\left(\frac{\partial v}{\partial \boldsymbol{\zeta}}\right) = \frac{\partial\left(F_k(v) e^{jk\zeta_2}\right)}{\partial \boldsymbol{\zeta}} e^{-jk\zeta_2} \text{ and } F_l\left(\frac{\partial u}{\partial \boldsymbol{\zeta}}\right) = \frac{\partial\left(F_l(u) e^{jl\zeta_2}\right)}{\partial \boldsymbol{\zeta}} e^{-jl\zeta_2}. \tag{A-7}$$

Defining

$$d_l^k\left(F_l(u), F_k(v)\right) := < F_k\left(\frac{\partial v}{\partial \boldsymbol{\zeta}}\right), F_{k-l}\left(\bar{\bar{\boldsymbol{\sigma}}}_{NEW}\right) F_l\left(\frac{\partial u}{\partial \boldsymbol{\zeta}}\right) >_{L^2(\Omega_{2D})}, \tag{A-8}$$

and

$$l_k(F_k(v)) := < F_k(v), F_k(f_{NEW}) >_{L^2(\Omega_{2D})} + < F_k(v), F_k(g_{NEW}) >_{L^2(\Gamma_N(\Omega_{2D}))}, \tag{A-9}$$

and considering that $d_l^k(F_l(u), F_k(v))$ is a bilinear form, from formula A-6 we obtain:

$$\begin{cases} \text{Find } u = \sum_l F_l\left(u_D\right) e^{jl\zeta_2} + H_D^1(\Omega) \text{ such that:} \\ \sum_{l=k-2}^{l=k+2} d_l^k\left(\,\cdot\,, F_k(v)\right) F_l(u) = \sum_{l=k-2}^{l=k+2} d_l^k F_l(u) = l_k(F_k(v)) \quad \forall F_k(v) e^{jk\zeta_2} \in H_D^1(\Omega), \end{cases} \tag{A-10}$$

Therefore, formula A-10 can be expressed in matrix form if we consider, for instance, the case of nine Fourier modes (namely, $k = -4, -3, \ldots, 3, 4$), as

$$\begin{bmatrix} d_{-4}^{-4} & d_{-3}^{-4} & d_{-2}^{-4} & 0 & 0 & 0 & 0 & 0 & 0 \\ d_{-4}^{-3} & d_{-3}^{-3} & d_{-2}^{-3} & d_{-1}^{-3} & 0 & 0 & 0 & 0 & 0 \\ d_{-4}^{-2} & d_{-3}^{-2} & d_{-2}^{-2} & d_{-1}^{-2} & d_0^{-2} & 0 & 0 & 0 & 0 \\ 0 & d_{-3}^{-1} & d_{-2}^{-1} & d_{-1}^{-1} & d_0^{-1} & d_1^{-1} & 0 & 0 & 0 \\ 0 & 0 & d_{-2}^{0} & d_{-1}^{0} & d_0^{0} & d_1^{0} & d_2^{0} & 0 & 0 \\ 0 & 0 & 0 & d_{-1}^{1} & d_0^{1} & d_1^{1} & d_2^{1} & d_3^{1} & 0 \\ 0 & 0 & 0 & 0 & d_0^{2} & d_1^{2} & d_2^{2} & d_3^{2} & d_4^{2} \\ 0 & 0 & 0 & 0 & 0 & d_1^{3} & d_2^{3} & d_3^{3} & d_4^{3} \\ 0 & 0 & 0 & 0 & 0 & 0 & d_2^{4} & d_3^{4} & d_4^{4} \end{bmatrix} \begin{bmatrix} F_{-4}(u) \\ F_{-3}(u) \\ F_{-2}(u) \\ F_{-1}(u) \\ F_0(u) \\ F_1(u) \\ F_2(u) \\ F_3(u) \\ F_4(u) \end{bmatrix} = \begin{bmatrix} l_{-4} \\ l_{-3} \\ l_{-2} \\ l_{-1} \\ l_0 \\ l_1 \\ l_2 \\ l_3 \\ l_4 \end{bmatrix}. \tag{A-11}$$

The resulting stiffness matrix (**A**) in equation A-11 is, in general, penta-diagonal. Furthermore, if we consider only subdomain III, **A** becomes tri-diagonal since $F_{k-l}(\overline{\overline{\boldsymbol{\sigma}}}_{NEW}) = 0$ for every $|\, k - l \,| > 1$ while, for subdomain I, **A** is diagonal since $F_{k-l}(\overline{\overline{\boldsymbol{\sigma}}}_{NEW}) = 0$ for if $|\, k - l \,| \neq 0$ (Pardo et al., 2008).

REFERENCES

Anderson, B. I., 2001, Modeling and inversion methods for the interpretation of resistivity logging tool response: Ph.D. thesis, Delft University of Technology.

Aris, R., 1962, Vectors, tensors, and the basic equations of fluid mechanics: Prentice Hall.

Avdeev, D. B., A. V. Kuvshino, O. V. Pankratov, and G. A. Newman, 2002, Three-dimensional induction logging problems, Part 1: An integral equation solution and model comparisons: Geophysics, **67**, 413-426.

Chen, Y. H., W. C. Chew, and G. J. Zhang, 1998, A novel array laterolog method: The Log Analyst, **39**, 22-33.

Cozzolino, K., and J. C. Silva, 2007, Synthetic focusing and simulation of dual laterolog tool in axisymmetric subsurface models: Journal of Applied Geophysics, **61**, 102-110.

Davydycheva, S., V. Druskin, and T. Habashy, 2003, An efficient finite-difference scheme for electromagnetic logging in 3D anisotropic inhomogeneous media: Geophysics, **68**, 1525-1536.

Demkowicz, L., 2007, Computing with hp-adaptive finite elements, v. 1: Chapman and Hall/CRC.

Demkowicz, L., J. Kurtz, D. Pardo, M. Paszynski, W. Rachowicz, and A. Zdunek, 2008, Computing with hp-adaptive finite elements, v. 2: Chapman and Hall/CRC.

Doll, H. G., 1951, The laterolog: A new resistivity logging method with electrodes using an automatic focusing system: Petroleum Transactions, AIME, **192**, 305-316.

Druskin, V. L., L. A. Knizhnerman, and P. Lee, 1999, New spectral Lanczos decomposition method for induction modeling in arbitrary 3D geometry: Geophysics, **64**, 701-706.

Liu, Z., J. Oyang, and J. Zhang, 1999, Dynamic dual-laterolog responses: Model and field applications in the Bohai Gulf of China: Journal of Petroleum Science and Engineering, **23**, 1-11.

Lovell, J. R., 1993, Finite element methods in resistivity logging: Ph.D. thesis, Delft University of Technology.

Newman, G. A., and D. L. Alumbaugh, 2002, Three-dimensional induction logging problems, part 2: A finite-difference solution: Geophysics, **67**, 484-491.

Pardo, D., L. Demkowicz, C. Torres-Verdín, and L. Tabarovsky, 2006, A goal-oriented hp-adaptive finite element method with electromagnetic applications. Part I: Electrostatics: International Journal for Numerical Methods in Engineering, **65**, 1269-1309.

Pardo, D., V. M. Calo, C. Torres-Verdín, and M. J. Nam, 2008, Fourier series expansion in a non-orthogonal system of coordinates for simulation of 3D DC borehole resistivity measurements: Computer Methods in Applied Mechanics and Engineering, **197**, 1906-1925.

Paszynski, M., L. Demkowicz, and D. Pardo, 2005, Verification of goal-oriented hp-adaptivity: Computers and Mathematics with Applications, **50**, 1395-1404.

Yang, W., C. Torres-Verdín, R. Akkurt, S. al-Dossari, A. Al-Towijri, and H. Ersoz, 2007, Interpretation of frequency-dependent dual laterolog measurements acquired in Middle-East carbonate reservoirs using a second-order finite element method: 48th Annual Symposium, SPWLA, Expanded Abstracts.

Wang, T., and J. Signorelli, 2004, Finite-difference modeling of electromagnetic tool response for logging while drilling: Geophysics, **69**, 152-160.

Table 1. Effects of anisotropy on LLd and LLs measurements simulated at the center of the third and fourth layers for angles of well deviation equal to 0°, 45°, and 60°. The corresponding effects are described in relative percent differences with respect to DLL readings simulated in the isotropic formation.

Mode	LLd			LLs		
Dip angle	0°	45°	60°	0°	45°	60°
Effect of anisotropy in third layer (%)	29.8	69.2	125.9	39.6	71.0	101.9
Effect of anisotropy in fourth layer (%)	−7.9	2.6	25.9	30.5	52.5	74.4

Figures Captions

Figure 1. Configuration of a commercial DLL tool with five current (A_0, A_1, $A_{1'}$, A_2, and $A_{2'}$) and four monitoring electrodes (M_1, $M_{1'}$, M_2, and $M_{2'}$). Dashed light gray lines indicate patterns of current flow for deep-sensing (LLd, left of panel) and shallow-sensing modes (LLs, right of panel).

Figure 2. (a) Cross section showing a deviated well with a dip angle of θ penetrating a layered formation. The horizontal circle in (a) indicates the "quasi-azimuthal" direction ζ_2 in a nonorthogonal system of coordinates, whereas both the x_3- (in Cartesian system of coordinates) and ζ_3-directions (in the nonorthogonal system of coordinates) correspond to the direction of the borehole. (b) In the nonorthogonal system, we employ three domains that have different systems of coordinates as described in the cross section corresponding to $\zeta_2 = 0$. Subdomain 1, which includes the DLL logging instrument, is part of the borehole, while subdomain 3 corresponds to the formation. Subdomain 2, the remainder part of the borehole not contained in subdomain 1, and it "glues" subdomain 1 with subdomain 3 so that the resulting system of coordinates is globally continuous, bijective, and with a positive Jacobian.

Figure 3. Comparisons of DLL apparent resistivities computed by Cozzolino et al. (2007) and with the 2D hp-FEM with the embedded post processing method (EPPM). Borehole radius and resistivity are equal to 0.1 m and 5 ohm-m, respectively. Straight solid lines describe layer resistivities, equal to 1, 0.1, and 10 ohm-m from top to bottom, respectively. A dashed line and open left triangles identify DLL readings simulated with the 2D hp-FEM from this study and by Cozzolino et al. (2007), respectively, for (a) LLd and (b) LLs modes. DLL apparent resistivities from Cozzolino et al. (2007) were digitized from those shown in their publication.

Figure 4. Formation including five horizontal layers of resistivities equal to 100, 5, 1000, 0.5, and 100 ohm-m from top to bottom, respectively, used as base model for the numerical simulations considered in this paper. The thicknesses of the second, third, and fourth layers (from top to bottom) are 2, 4, and 3 m, respectively. Borehole radius and resistivity are equal to 0.1 m and 0.1 ohm-m, respectively. Either invasion or electrical anisotropy is included in the third and fourth layers. The symbol R describes radial length of invasion.

Figure 5. Comparison of calculated apparent resistivities for a vertical well penetrating the five-layer formation model (Figure 4) with and without presence of invasion. Straight solid and dashed black lines describe resistivities of layers and invaded zones, respectively. Dashed lines, diamonds, and triangles in black identify LLd apparent resistivities for 0, 0.1, and 0.8 m radial lengths of invasion (R), respectively, and those in light gray identify LLs apparent resistivities.

Figure 6. Final adapted hp-grid for a LLd measurement simulated at a depth of 4 m for a vertical well penetrating the five-layer formation model (Figure 4) without presence of invasion. Figures show progressive amplifications by factors of 1, 10, and 100, respectively (from left), toward a

singularity located at (ρ = 0.1 m, z = 4 m), where the borehole (0.1 ohm-m), the third (1000 ohm-m), and the fourth layers (0.5 ohm-m) meet. Different colors indicate different polynomial orders of approximation (p), ranging from p = 1 (lighter) to p = 8 (darker).

Figure 7. Comparison of calculated apparent resistivities for a vertical well penetrating isotropic and anisotropic formations composed of five horizontal layers (Figure 4). For the isotropic case, layer resistivities are 100, 5, 1000, 0.5, and 100 ohm-m from top to bottom, respectively. For the anisotropic case, only the third and fourth layers are electrically anisotropic, with vertical resistivities equal to 10000 and 50 ohm-m, respectively. Straight solid and dashed lines identify horizontal and vertical layer resistivities, respectively. The dashed line and diamonds in black identify LLd apparent resistivities calculated for isotropic and anisotropic formations, respectively, and those in light gray identify LLs apparent resistivities.

Figure 8. Description of a formation model used for verification of the 3D hp FEM. The model is composed of a homogeneous formation with a resistivity equal to 1 ohm-m or 1000 ohm-m and a borehole with a resistivity equal to 0.1 ohm-m and a radius of 0.1 m. Dip angle, θ, is set to 0°, 30°, and 60°.

Figure 9. Convergence behavior as a function of the number of Fourier modes used in the simulation of both LLd and LLs measurements in deviated wells penetrating a formation with resistivity equal to (a) 1 or (b) 1000 ohm-m. Solid and dashed curves describe DLL measurements simulated for 30° and 60° deviated wells, respectively, and black and light-gray curves describe simulated LLd and LLs measurements, respectively.

Figure 10. Simulation of LLd apparent resistivities as a function of the number of Fourier modes for a 45° deviated well penetrating the five-layer formation model (Figure 4). The number of Fourier modes under consideration is one, three, five, and seven (panels a, b, c, and d, respectively) when computing LLd apparent resistivities. LLd apparent resistivities computed with nine Fourier modes are regarded as the fully converged solution. A straight solid line describes the layer resistivities.

Figure 11. Comparison of apparent resistivities calculated for vertical and deviated wells penetrating the five-layer formation model (Figure 4). A straight solid line describes the layer resistivities. The dashed line, diamonds, and triangles in black identify LLd apparent resistivities for 0°, 10°, 45°, and 60° deviated wells, respectively, and those in light gray identify shallow LLs apparent resistivities.

Figure 12. Comparison of apparent resistivities calculated for 0° and 45° deviated wells (panels a and b, respectively) and for 45° and 60° deviated wells (panels c and d, respectively) with and without invaded zones (the radial length of invasion is 0.1 m) in the third and fourth layers. Straight solid and dashed lines describe resistivities of layers and invaded zones, respectively. Dashed line and diamonds identify simulated apparent resistivities in virgin and invaded formations, respectively, for LLd (panels a and c) and LLs (panels b and d) modes.

Figure 13. Comparison of apparent resistivities calculated for (panel a) 45° and (panel b) 60° deviated wells penetrating isotropic and anisotropic formations composed of five horizontal layers (Figure 4). Straight solid and dashed lines describe horizontal and vertical layer resistivities, respectively. Dashed line and diamonds in black identify simulated LLd apparent resistivities for isotropic and anisotropic formations, respectively, while those in light gray identify LLs simulated apparent resistivities.

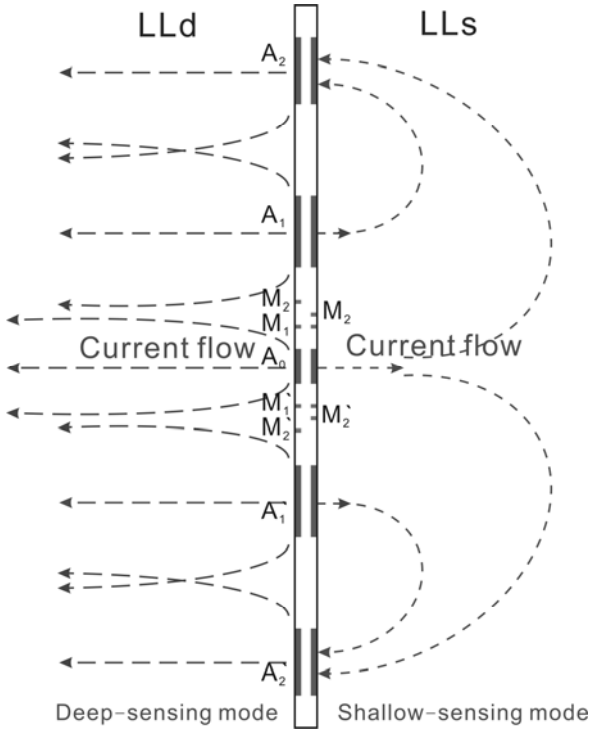
LLd
LLs
A2
A1
M2
M1
A0
M1`
M2`
A1`
A2`
Current flow
Current flow
Deep-sensing mode
Shallow-sensing mode

Figure 1.

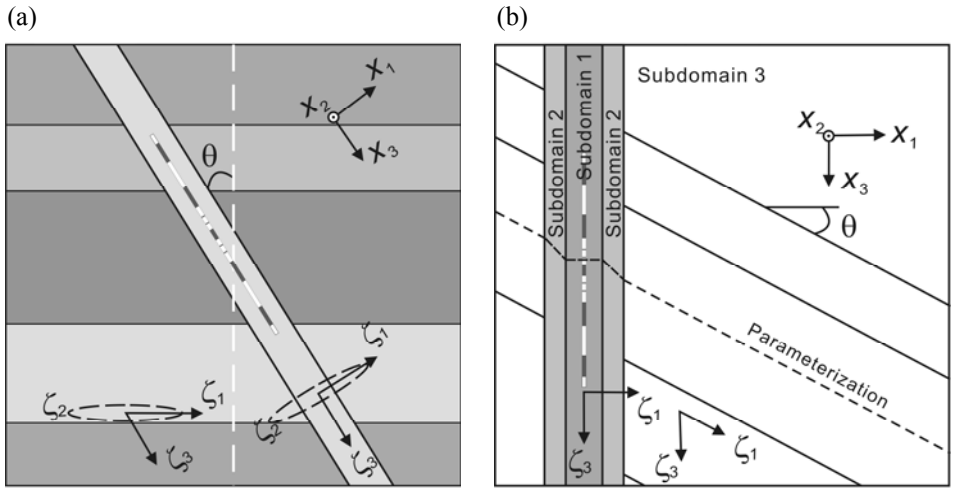
(a)
(b)
θ
Subdomain 1
Subdomain 2
Subdomain 2
Subdomain 3
Parameterization

Figure 2.

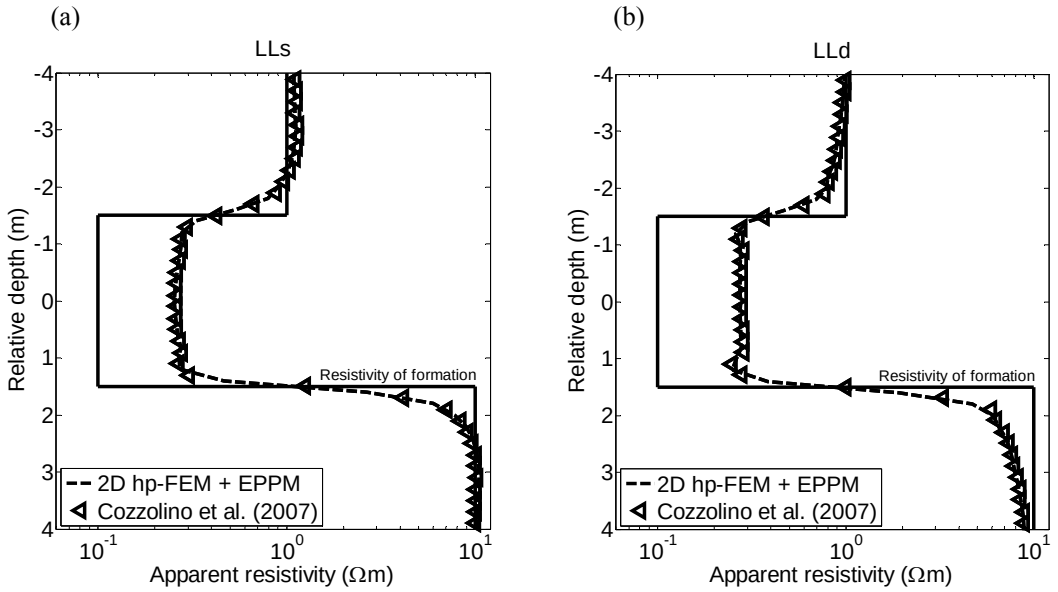
(a)
LLs
Relative depth (m)
Resistivity of formation
2D hp-FEM + EPPM
Cozzolino et al. (2007)
Apparent resistivity (Ωm)
(b)
LLd
Relative depth (m)
Resistivity of formation
2D hp-FEM + EPPM
Cozzolino et al. (2007)
Apparent resistivity (Ωm)

Figure 3.

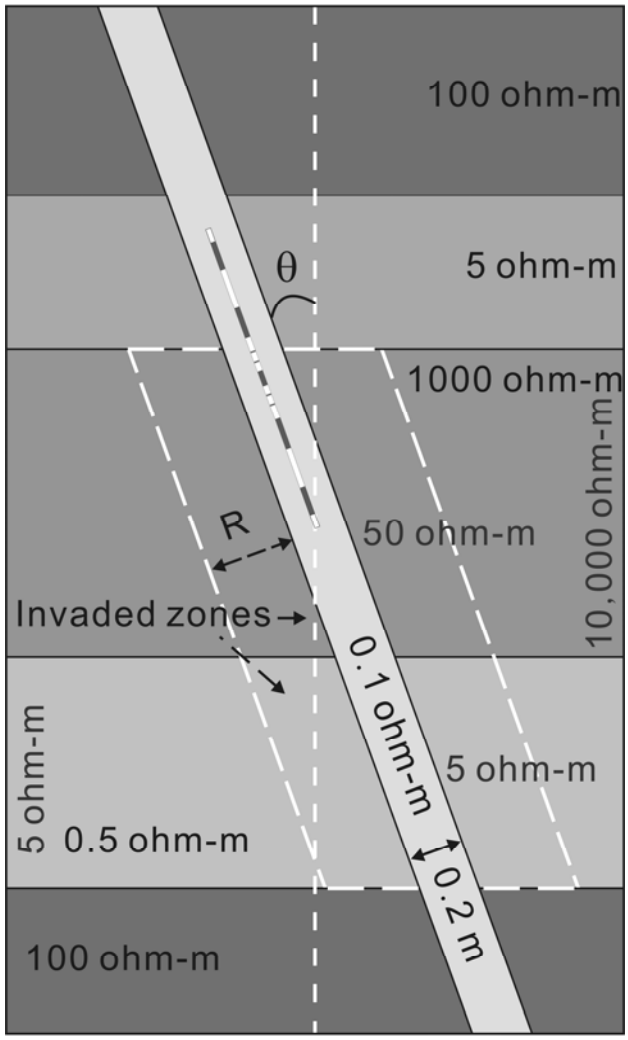
100 ohm-m
5 ohm-m
θ
1000 ohm-m
10,000 ohm-m
R
50 ohm-m
Invaded zones
0.1 ohm-m
0.2 m
5 ohm-m
5 ohm-m
0.5 ohm-m
100 ohm-m

Figure 4.

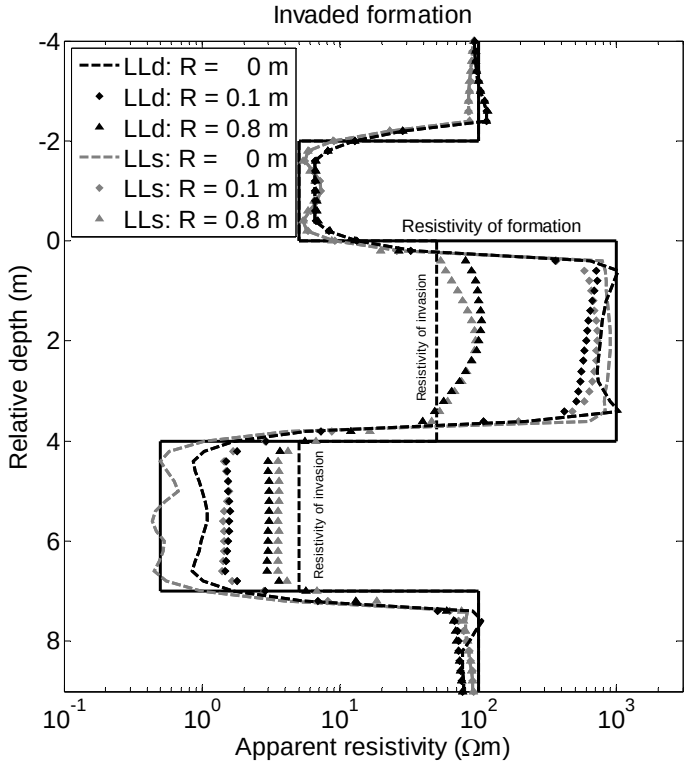
Invaded formation
LLd: R = 0 m
LLd: R = 0.1 m
LLd: R = 0.8 m
LLs: R = 0 m
LLs: R = 0.1 m
LLs: R = 0.8 m
Resistivity of formation
Resistivity of invasion
Resistivity of invasion
Relative depth (m)
Apparent resistivity (Ωm)

Figure 5.

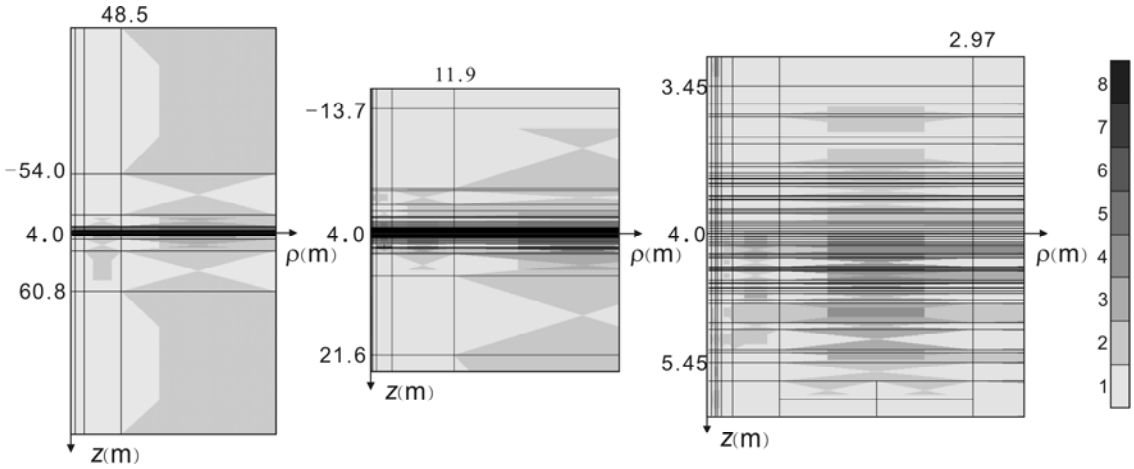
48.5
−54.0
4.0
60.8
z(m)
ρ(m)
11.9
−13.7
4.0
21.6
z(m)
ρ(m)
2.97
3.45
4.0
5.45
z(m)
ρ(m)
8
7
6
5
4
3
2
1
Figure 6.

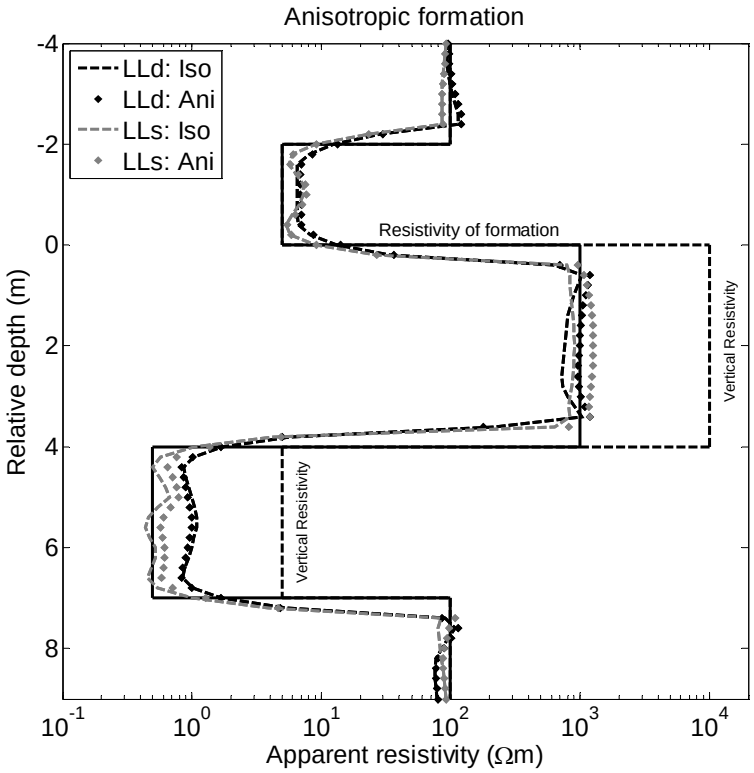
Anisotropic formation
LLd: Iso
LLd: Ani
LLs: Iso
LLs: Ani
Resistivity of formation
Vertical Resistivity
Vertical Resistivity
Relative depth (m)
Apparent resistivity (Ωm)
-4
-2
0
2
4
6
8
10^-1
10^0
10^1
10^2
10^3
10^4

Figure 7.

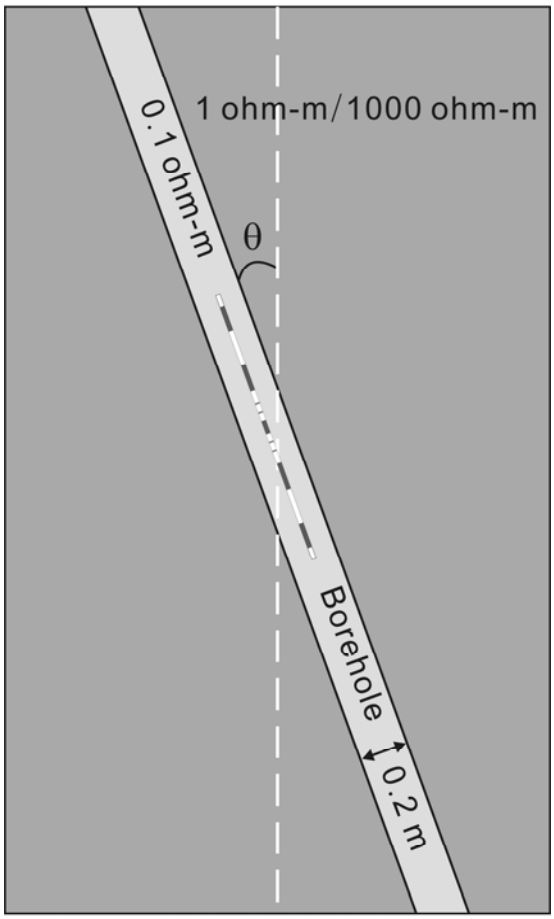

Figure 8.

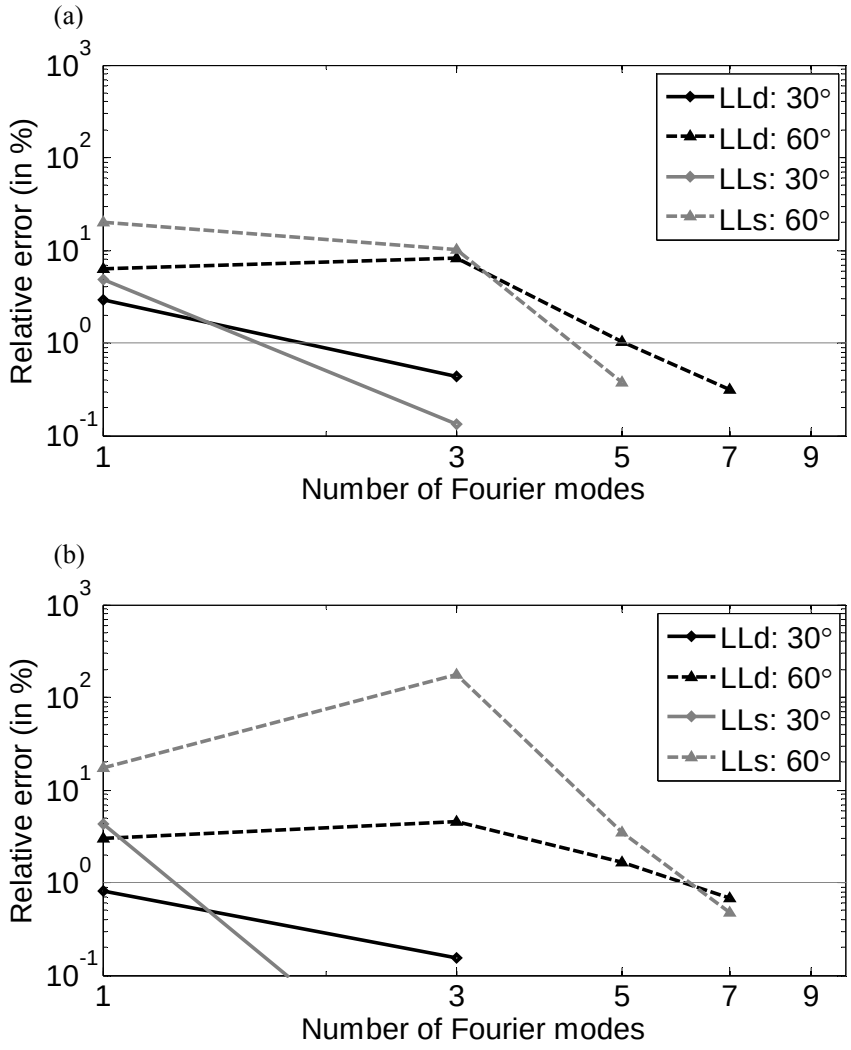
(a)
Relative error (in %)
Number of Fourier modes
LLd: 30°
LLd: 60°
LLs: 30°
LLs: 60°
(b)
Relative error (in %)
Number of Fourier modes
LLd: 30°
LLd: 60°
LLs: 30°
LLs: 60°

Figure 9.

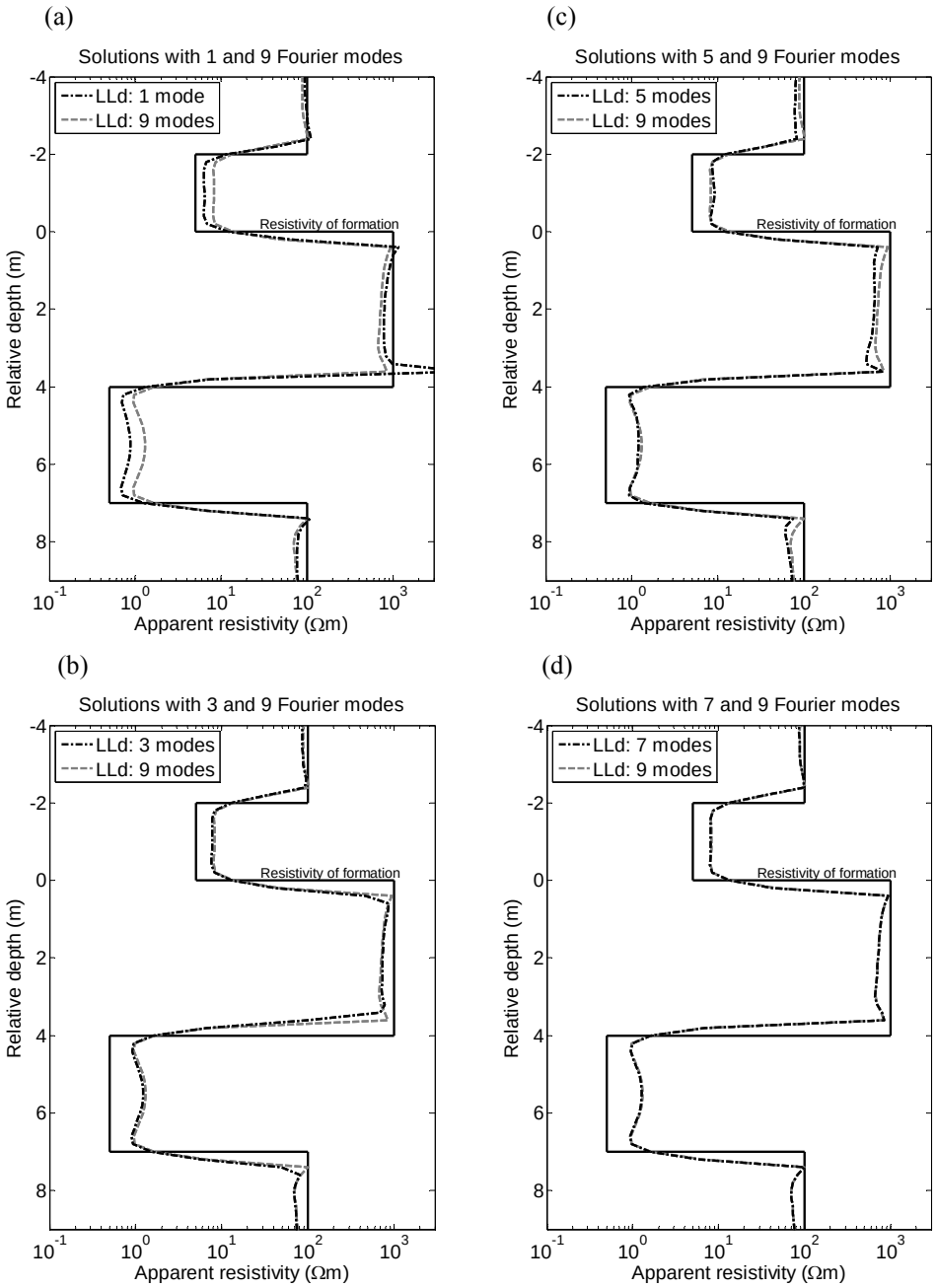
(a)
Solutions with 1 and 9 Fourier modes
LLd: 1 mode
LLd: 9 modes
Resistivity of formation
Relative depth (m)
Apparent resistivity (Ωm)
(c)
Solutions with 5 and 9 Fourier modes
LLd: 5 modes
LLd: 9 modes
Resistivity of formation
Relative depth (m)
Apparent resistivity (Ωm)
(b)
Solutions with 3 and 9 Fourier modes
LLd: 3 modes
LLd: 9 modes
Resistivity of formation
Relative depth (m)
Apparent resistivity (Ωm)
(d)
Solutions with 7 and 9 Fourier modes
LLd: 7 modes
LLd: 9 modes
Resistivity of formation
Relative depth (m)
Apparent resistivity (Ωm)

Figure 10.

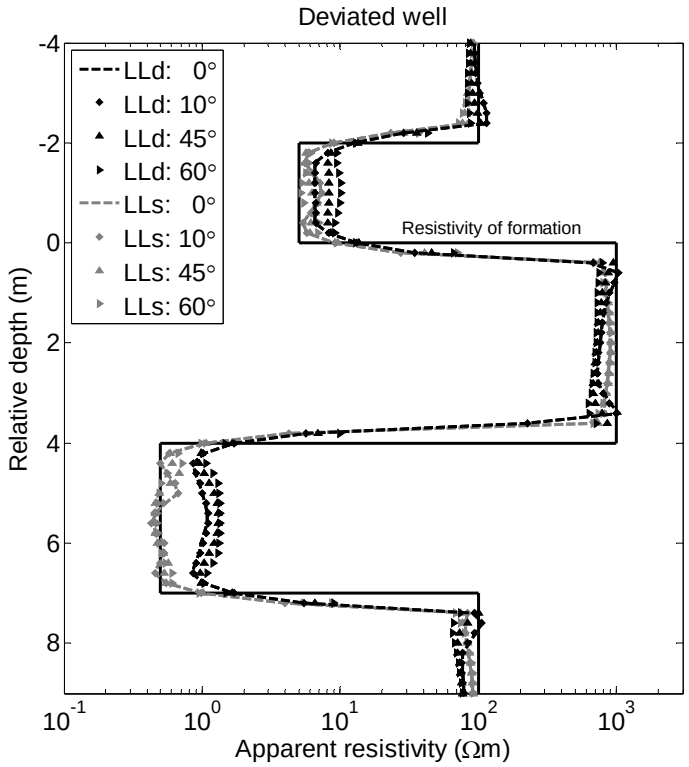
Deviated well
LLd: 0°
LLd: 10°
LLd: 45°
LLd: 60°
LLs: 0°
LLs: 10°
LLs: 45°
LLs: 60°
Resistivity of formation
Relative depth (m)
Apparent resistivity (Ωm)
-4
-2
0
2
4
6
8
10^-1
10^0
10^1
10^2
10^3

Figure 11.

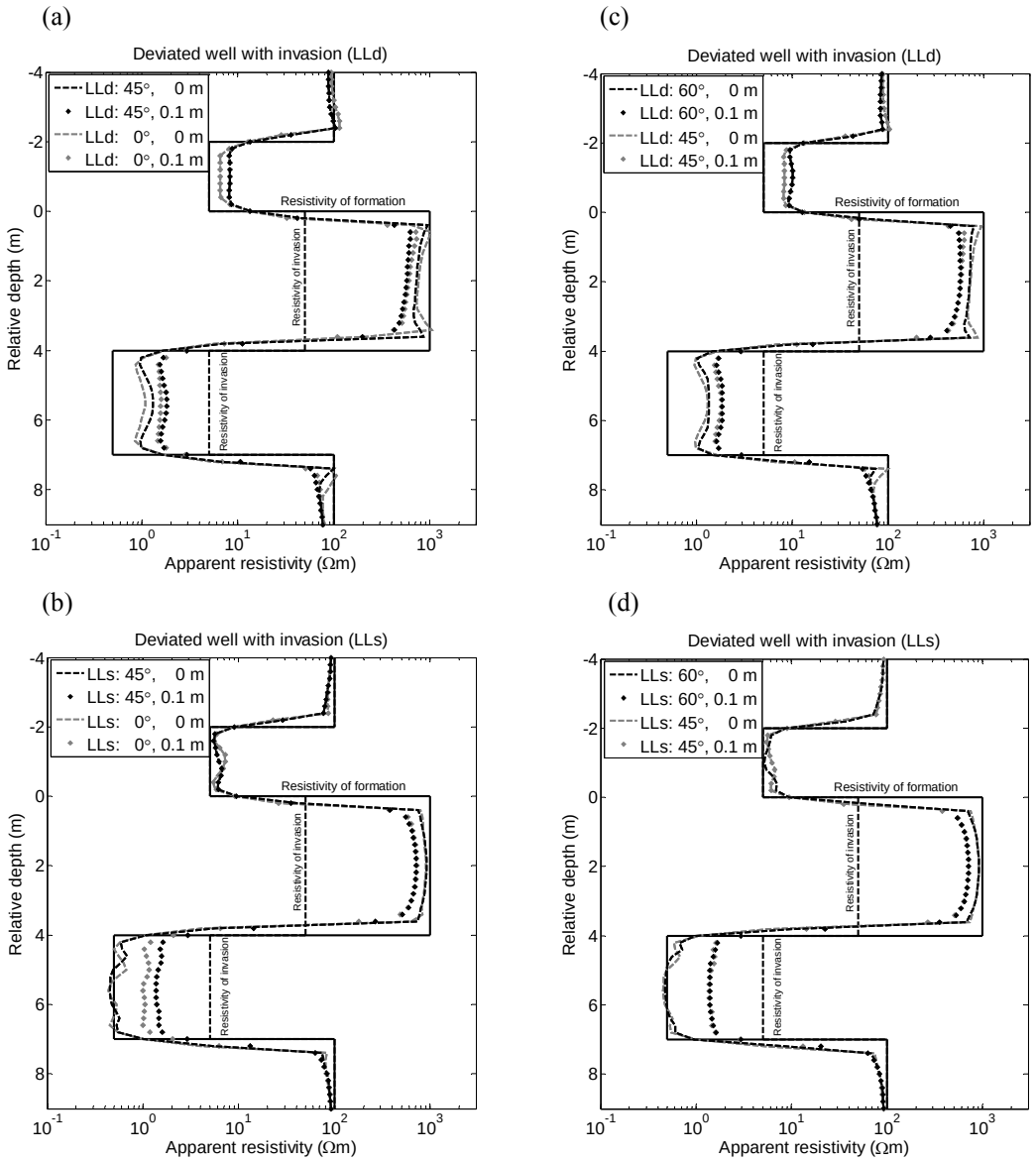
(a)
Deviated well with invasion (LLd)
LLd: 45°, 0 m
LLd: 45°, 0.1 m
LLd: 0°, 0 m
LLd: 0°, 0.1 m
Resistivity of formation
Resistivity of invasion
Resistivity of invasion
Relative depth (m)
Apparent resistivity (Ωm)
(c)
Deviated well with invasion (LLd)
LLd: 60°, 0 m
LLd: 60°, 0.1 m
LLd: 45°, 0 m
LLd: 45°, 0.1 m
Resistivity of formation
Resistivity of invasion
Resistivity of invasion
Relative depth (m)
Apparent resistivity (Ωm)
(b)
Deviated well with invasion (LLs)
LLs: 45°, 0 m
LLs: 45°, 0.1 m
LLs: 0°, 0 m
LLs: 0°, 0.1 m
Resistivity of formation
Resistivity of invasion
Resistivity of invasion
Relative depth (m)
Apparent resistivity (Ωm)
(d)
Deviated well with invasion (LLs)
LLs: 60°, 0 m
LLs: 60°, 0.1 m
LLs: 45°, 0 m
LLs: 45°, 0.1 m
Resistivity of formation
Resistivity of invasion
Resistivity of invasion
Relative depth (m)
Apparent resistivity (Ωm)

Figure 12.

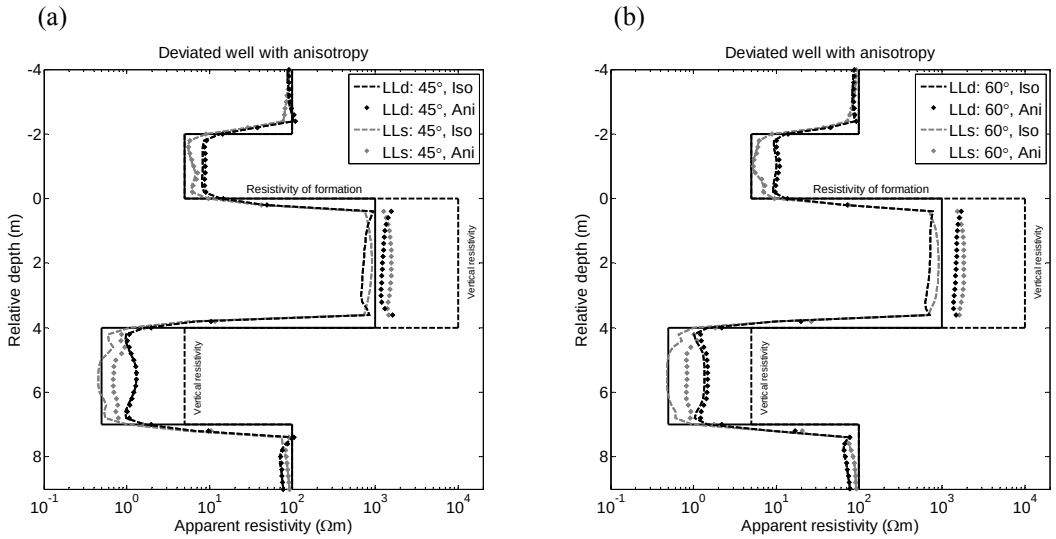
(a)
Deviated well with anisotropy
LLd: 45°, Iso
LLd: 45°, Ani
LLs: 45°, Iso
LLs: 45°, Ani
Resistivity of formation
Vertical resistivity
Vertical resistivity
Relative depth (m)
Apparent resistivity (Ωm)
(b)
Deviated well with anisotropy
LLd: 60°, Iso
LLd: 60°, Ani
LLs: 60°, Iso
LLs: 60°, Ani
Resistivity of formation
Vertical resistivity
Vertical resistivity
Relative depth (m)
Apparent resistivity (Ωm)

Figure 13.